

Testing subhalo abundance matching from redshift-space clustering

Mikito Yamamoto,¹ Shogo Masaki² and Chiaki Hikage³

¹ *Department of Physics, Nagoya University, Aichi 464-8602, Japan*

² *NTT Secure Platform Laboratories, NTT Corporation, Tokyo 180-8585, Japan*

³ *Kobayashi Maskawa Institute (KMI), Nagoya University, Aichi 464-8602, Japan*

23 March 2021

ABSTRACT

We present a first application of the subhalo abundance matching (SHAM) method to describe the redshift-space clustering of galaxies including the non-linear redshift-space distortion, i.e., the Fingers-of-God. We find that the standard SHAM connecting the luminosity of galaxies to the maximum circular velocity of subhalos well reproduces the luminosity dependence of redshift-space clustering of galaxies in the Sloan Digital Sky Survey in a wide range of scales from 0.3 to 40 h^{-1} Mpc. The result indicates that the SHAM approach is very promising for establishing a theoretical model of redshift-space galaxy clustering without additional parameters. We also test color abundance matching using two different proxies for colors: subhalo age and local dark matter density following the method by Masaki et al. (2013b). Observed clustering of red galaxies exhibits much stronger Fingers-of-God effect than blue galaxies. We find that the subhalo age model describes the observed color-dependent redshift-space clustering much better than the local dark matter density model. The result infers that the age of subhalos is a key ingredient to determine the color of galaxies.

Key words: galaxies: formation – galaxies: haloes – galaxies: statistics cosmology: observations – cosmology: large-scale structure of Universe

1 INTRODUCTION

Establishing connection between the properties of galaxies and the underlying dark matter is crucial for both studies of galaxy evolution and cosmology. Star formation histories of galaxies has been studied by associating galaxies with their host dark matter halos and their connection provides fundamental constraints on galaxy formation models (e.g., Conroy & Wechsler 2009; Leauthaud et al. 2010; Behroozi et al. 2013). Future galaxy surveys such as Prime Focus Spectrograph (PFS) (Takada et al. 2012), the Dark Energy Spectroscopic Instrument (DESI) (Levi et al. 2013), *Euclid* (Lau-reijs et al. 2011) and *the Wide Field Infrared Survey Telescope (WFIRST)* (Spergel et al. 2013) use both luminous red galaxies and emission line galaxies to trace the large-scale structure at $z \lesssim 2$. A major uncertainty for the precision cosmology using galaxy surveys comes from the challenge of relating galaxies and dark matter.

Subhalo abundance matching (SHAM) is a promising approach to relate the properties of galaxies to dark matter subhalos (e.g., Kravtsov et al. 2004; Nagai & Kravtsov 2005; Conroy et al. 2006). The simple abundance matching model by assigning luminosity in the order of the maximum circular velocity of dark matter subhalos successfully reproduces the galaxy clustering at different redshifts (Conroy et al. 2006). Masaki et al. (2013a) also finds a good abundance matching between the progenitor halos of luminous red galaxies (LRGs) and the massive halos at $z \sim 2$ and then explains the clustering properties of LRGs very well. There also has been recent attempts to relate the galaxy color to the subhalo prop-

erties, i.e., color abundance matching. Galaxy color reflects the activity of on-going star formation: red galaxies consists of aged stars and the star formation is quenched, whereas blue galaxies are relatively young and their star formation is active. It is also known that redder galaxies live in denser environments via the measurement of galaxy clustering (Norberg et al. 2002; Zehavi et al. 2005; Coil et al. 2008; Guo et al. 2014; Skibba et al. 2014) and also from the color-density relation (Balogh et al. 2004; Cooper et al. 2006; Blanton & Berlind 2007; Bamford et al. 2009). Masaki et al. (2013b) extends a SHAM technique to explain color-dependent properties of galaxy clustering as well as galaxy-galaxy lensing using two proxies of color: one is the local dark matter density motivated by the environmental dependence of galaxy color; the other is the subhalo age reflecting the different aged population between red and blue galaxies. Hearin & Watson (2013) also perform color abundance matching by assigning the redshift z_{starve} characterizing the epoch of star formation quenching to subhalos.

So far, the projected correlation function along the line-of-sight has been commonly used for testing SHAM to avoid the effect of redshift-space distortion (RSD) due to peculiar motion of galaxies. The velocity of galaxies within and outskirts of clusters is complicated and affected by different physics including the dynamical friction, tidal stripping/disruption, merging, and ram pressure. The internal motion of galaxies elongate the RSD of galaxies along the line-of-sight direction, known as Fingers-of-God (FoG; Jackson 1972). The FoG effect is clearly different by colors: red galaxies show much stronger FoG effect than blue galaxies (Zehavi

et al. 2005; Coil et al. 2008). In the framework of the halo model, the line-of-sight elongation in the galaxy distribution emerges from the one-halo term, which is the contribution of central-satellite and satellite-satellite galaxy pairs in the same halos (Hikage & Yamamoto 2013). The observed color difference of FoG feature mainly reflects the difference of the satellite fraction, radial profiles and their kinematics between red and blue galaxies.

In this paper we extend the SHAM approach to redshift space and test if the model describes the luminosity and color dependence of redshift-space galaxy clustering for the first time. We characterize the anisotropy of redshift-space galaxy clustering by a multipole expansion. High- l multipole components such as hexadecapole ($l = 4$) mainly generated from the FoG effect provide a useful probe of constraining the fraction and the internal velocity dispersions of satellite galaxies (Hikage 2014). In our analysis, we focus on the non-linear scales from subMpc to ~ 1 Mpc where the difference of the FoG effect can be clearly seen. Extending SHAM to redshift space is an important step for establishing a theoretical model of the redshift-space clustering with a small number of parameters. The coherent bulk motion of galaxies induced by gravitational evolution squashes the distribution of galaxies along the line-of-sight direction (Kaiser 1987; Hamilton 1992; Peacock et al. 2001). The anisotropy in the clustering provides a good probe of cosmic growth rate and have been used for testing gravity (e.g. Guzzo et al. 2008; Yamamoto et al. 2008, 2010; Beutler et al. 2014). Very recently Hearin (2015) points out the impact of the assembly bias using color abundance matching technique and shows that the simple formalism of halo occupation distribution causes a significant systematics in RSD studies using pairwise velocity statistics.

The paper is summarized as follows: in Section 2, we explain the details of the observational catalogs and subhalo samples used in our analysis. We also make a brief summary of the two color assignment schemes based on the subhalo age and local dark matter density. In Section 3, we show the results of the luminosity and color dependence of observed redshift-space clustering compared with those of subhalos. and test SHAM and two color assignment methods. We discuss what causes the difference of the two color assignment methods. Section 4 is devoted to summary and conclusions.

2 OBSERVATION AND SUBHALO SAMPLES

2.1 Observational data

We use the magnitude-limited samples of the Sloan Digital Sky Survey (SDSS) Data Release 7 galaxies (Abazajian et al. 2009) in three different luminosity bins: $-22 < M_r < -21$, $-21 < M_r < -20$, and $-20 < M_r < -19$ where M_r is the r-band absolute magnitude including $-5 \log h$ term. The apparent magnitude m_r ranges from 14.5 to 17.6 based on the Petrosian magnitude and K -corrected to rest-frame magnitude at $z = 0.1$. The galaxy color is divided into red and blue on the K -corrected $g - r$ color and r -band apparent magnitude plane: red when $g - r > 0.21 - 0.03M_r$, otherwise blue (see the details of the samples in Zehavi et al. 2011). The fractions of red galaxies become 0.63, 0.53, and 0.43 from luminous to faint magnitude samples. Due to the physical size of the spectroscopic fiber, both spectra of adjacent galaxies with the angular separation less than 55 arcmin cannot be measured simultaneously, i.e., “fiber collision effect”. This corresponds to the projected comoving scale $r_p = 0.12 h^{-1}$ Mpc at the outer edge of the sample. In our analysis, we focus on the range of scales where the fiber collision effect is unimportant.

2.2 Subhalo catalogs and color assignment

We use the subhalo samples corresponding to the magnitude ranges of the observational samples. Below we summarize the catalogs briefly (see the details in Masaki et al. 2013b). The subhalo catalogs are constructed from N -body simulations using publicly available code GADGET-2 (Springel et al. 2001b; Springel 2005). The initial condition is a random-Gaussian field with the power spectrum based on a flat Λ cold dark matter model of the *Wilkinson Microwave Anisotropy Probe (WMAP)* 7-year results (Komatsu et al. 2011): $\Omega_m = 0.272$, $\Omega_b = 0.0441$, $\Omega_\Lambda = 0.728$, $H_0 = 100h = 70.2 \text{ km s}^{-1}\text{Mpc}^{-1}$, $\sigma_8 = 0.807$, and $n_s = 0.961$. We employ 1024^3 dark matter (DM) particles in each cubic simulation box. We use two simulation boxes with the side length L_{box} and the redshift of output snapshot z_{out} depending on the range of magnitude as listed in Table 1.

Halos are identified using the Friends-of-Friends (FOF) algorithm with the linking length of 0.2 times the mean interparticle distance. Satellite subhalos, dense clumps within each halo, are identified using the SUBFIND algorithm with the minimum number of DM particles set to be 20 (Springel et al. 2001a). A central subhalo is defined as the rest of DM particles without satellite subhalos (and the ‘fuzz’ component). The central positions of both central and satellite subhalos are the density maximum rather than the center of mass, and then the velocity of a subhalo is given by the mean velocity of all inner particles. We neglect the inner velocity of central galaxies against the halo bulk velocity.

We assume the monotonic relation between the galaxy luminosity measured with M_r and the maximum circular velocity $V_{\text{max}}^{\text{acc}}$ to match their abundance as $n_{\text{gal}}(> L) = n_{\text{subhalo}}(> V_{\text{max}}^{\text{acc}})$ (Conroy et al. 2006). $V_{\text{max}}^{\text{acc}}$ is the maximum value of the circular velocity of particles $V_{\text{circ}}(R) = \sqrt{GM(< R)/R}$, where R is the distance from the center of each subhalo. The maximum circular velocity for a central subhalo is computed at the observed epoch, however, V_{max} for a satellite is computed at the accretion epoch because subhalos inside clusters lose their initial mass due to tidal stripping while the stellar mass is tightly bound (Nagai & Kravtsov 2005). Furthermore we divide each magnitude sample into red and blue colors based on the following two models (Masaki et al. 2013b).

(i) Subhalo age model (“Age model”)

The galaxy color reflects the age of the stellar population: red galaxies consist of old stellar population when the star formation is quenched, whereas blue galaxies consist of younger stellar population with active star formation. We assign the color by the subhalo formation epoch z_{form} , which is defined as the epoch when the maximum circular velocity of the subhalo first crosses some constant value f times $V_{\text{max}}^{\text{acc}}$:

$$V_{\text{max}}(z = z_{\text{form}}) = f \times V_{\text{max}}^{\text{acc}} \quad (0 < f < 1), \quad (1)$$

(ii) Local DM density model (“L.D. model”)

The other way of color assignment is based on the local DM density motivated by the observation that redder galaxies locate in denser environments (Zehavi et al. 2005; Mandelbaum et al. 2006). The local DM density $\rho(R_{\text{DM}})$ of each subhalo is estimated from the number of DM particles within the distance of R_{DM} from the subhalo center.

We assign color information with subhalos by assuming a monotonic relation with z_{form} , or $\rho(R_{\text{DM}})$ to match the red fraction of each observational sample. Followed by Masaki et al. (2013b), a constant factor f in the age model is set to be 0.9 for all magni-

Table 1. Basic information of subhalo catalogs for three magnitude samples: simulation box size L_{box} , the output redshift of simulation snapshot z_{out} , the number of subhalos N_{sub} matching to the observed number density, satellite fraction f_{sat} of red and blue subhalo catalogs in two color assignment models: subhalo age (Age model) and local DM density (L.D. model).

M_r	z_{out}	L_{box}	N_{sub}	f_{sat}				
				All	Age model		L.D. model	
					red	blue	red	blue
$[-22, -21]$	0.1	$300 h^{-1}\text{Mpc}$	29969	0.22	0.28	0.12	0.26	0.16
$[-21, -20]$	0	$200 h^{-1}\text{Mpc}$	43200	0.32	0.40	0.21	0.42	0.20
$[-20, -19]$	0	$200 h^{-1}\text{Mpc}$	81600	0.33	0.42	0.26	0.59	0.13

tude bins to agree with the projected clustering for both red and blue galaxies (Zehavi et al. 2011). The scale R_{DM} in the L.D. model is set to be $250 h^{-1}\text{kpc}$ for the most luminous sample of $-22 < M_r < -21$ and $200 h^{-1}\text{kpc}$ for the other samples.

The fraction of satellite galaxies play a significant role in the small-scale clustering because of their large internal motion compared to the central galaxies. Table 1 lists the satellite fraction $f_{\text{sat}} = N_{\text{sat}}/(N_{\text{cen}} + N_{\text{sat}})$ of red and blue samples in the two color assignment models. In both models, red galaxy samples have a larger f_{sat} than the blue sample. Luminous galaxy samples have smaller f_{sat} , which reflect that the luminous galaxy is more likely to be central galaxies rather than satellites. The difference of f_{sat} among the two color assignment models is small expect for the faintest sample where (smaller) satellite fraction of red (blue) galaxies in the L.D. model.

3 RESULTS

In this section, we show the result of the redshift-space clustering before and after color separation to see how SHAM and two color assignment models reproduce the observations. We use multipole correlation functions $\xi_l(l = 0, 2, 4)$ and focus on the non-linear gravitational scales from subMpc to ~ 10 Mpc scales.

3.1 Multipole correlation functions

We compute the redshift-space two-point correlation functions of observational galaxy samples using Landy & Szalay estimator (Landy & Szalay 1993)

$$\xi(s, \mu) = \frac{\text{DD} - 2\text{DR} + \text{RR}}{\text{RR}}, \quad (2)$$

where DD, DR, and RR is the number of data-data, data-random, and random-random pairs normalized by the total number of pairs at each bin of the three-dimensional distance of s and the cosine of the angle between the separation and the line-of-sight direction μ . Our bins of s is logarithmically equal from 0.32 to $40 h^{-1}\text{Mpc}$ with 11 bins.

The anisotropy of galaxy clustering in redshift space is described with the multipole expansion using Legendre polynomials:

$$\xi_l(s) = \frac{1}{2} \int_{-1}^1 d\mu \xi(s, \mu) \mathcal{L}_l(\mu), \quad (3)$$

where μ is the cosine of the angle to the line-of-sight direction and $\mathcal{L}_l(\mu)$ is the l -th Legendre polynomials: $\mathcal{L}_0(\mu) = 1$, $\mathcal{L}_2(\mu) = (3\mu^2 - 1)/2$, and $\mathcal{L}_4(\mu) = (35\mu^4 - 30\mu^2 + 3)/8$.

In our analysis, we focus on the monopole ($l = 0$), quadrupole ($l = 2$), and hexadecapole ($l = 4$) components. Coherent bulk motion of galaxies known as Kaiser effect squashes the redshift-space galaxy clustering along the line-of-sight direction and then the quadrupole component becomes negative. Kaiser effect on higher-order multipoles is small. On the other hand, the elongated distribution by the FoG effect generates high-order anisotropic components such as a hexadecapole and then both quadrupole and hexadecapole components have positive values (Hikage & Yamamoto 2013). As the FoG effect increases, their amplitude becomes larger.

Since both observational and simulated subhalo samples are one realization in each magnitude bin, we estimate the error of ξ_l using the Jackknife re-sampling method as follows:

$$\sigma_l^2(s) = \frac{N-1}{N} \sum_i^N [\xi_l^i(s) - \langle \xi_l(s) \rangle]^2, \quad (4)$$

where N is the number of subsamples, ξ_l^i denotes l -th multipole for the sample without data in i -th sub-volume, and $\langle \xi_l(s) \rangle$ represents the ensemble average of $\xi_l^i(s)$ over subsamples. In order to estimate the error, we divide each observational sample into 125 subsamples with equal sky area. Subhalo samples are also divided into $125(=5^3)$ sub-cubes with equal volume.

3.2 Luminosity dependence

First we show the comparison of redshift-space clustering before color separation between the observed galaxies and the SHAM-based subhalo samples. Fig. 1 shows the results of $\xi_l(s)(l = 0, 2, 4)$ for three magnitude samples. The errors of both the observations and the subhalo samples are estimated from the Jackknife resampling method. We find that the SHAM method well reproduces the luminosity dependence of redshift-space galaxy clustering without introducing additional parameters. The overall amplitude of ξ_l increases for more luminous samples because luminous galaxies are hosted by massive halos and has a larger galaxy biasing. One can find that ξ_2 and ξ_4 are suppressed on subMpc scales in the most luminous sample. This is because more luminous galaxies have a lower f_{sat} (see Table 1) and thereby the FoG anisotropy due to satellites becomes smaller. The agreement of ξ_l between the observations and the subhalos is particularly excellent for the intermediate magnitude sample. This indicates that the internal motion of satellites responsible for the FoG effect is well described by the motion of subhalos and then the SHAM approach can be a powerful tool for building a theoretical framework of redshift-space clustering. There is however a systematic difference that the brightest (faintest) galaxy sample has weaker (stronger) FoG effect than the subhalo sample. This may indicate the importance of baryonic physics such as hydrodynamic drag by the gas that

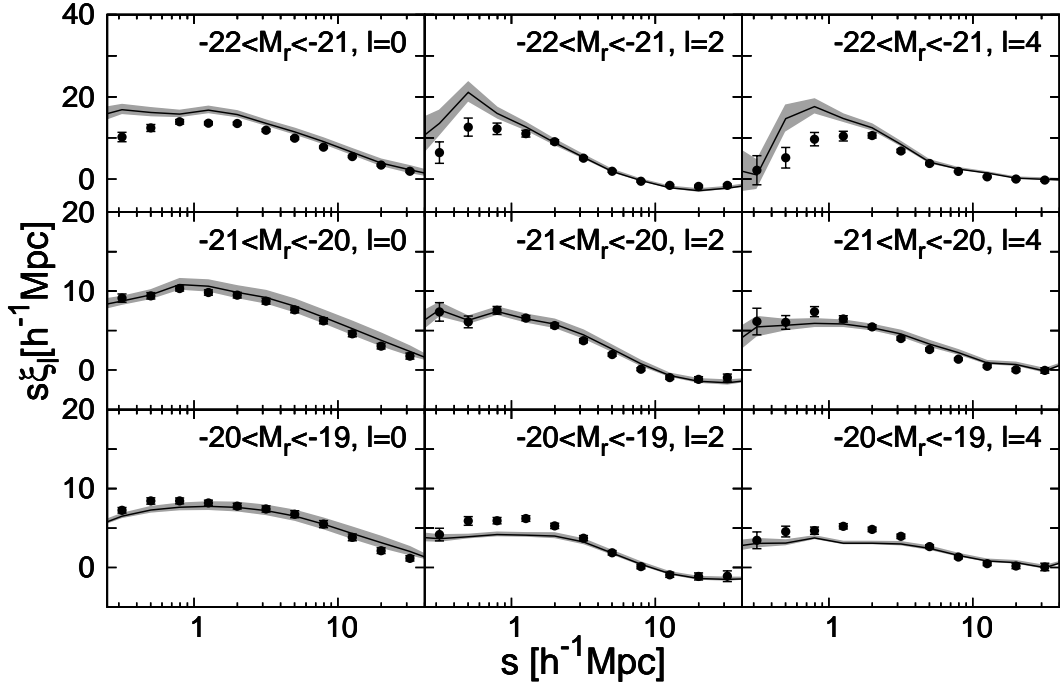


Figure 1. Comparison of the multipole correlation functions $s\xi_l(s)$ ($l = 0, 2, 4$ from left to right) between observations (symbols) and subhalo catalogs (lines) for three magnitude samples. The error-bars represent the 1σ dispersion estimated with the Jackknife resampling method. Multiplication by the radial scale s is for a visual purpose.

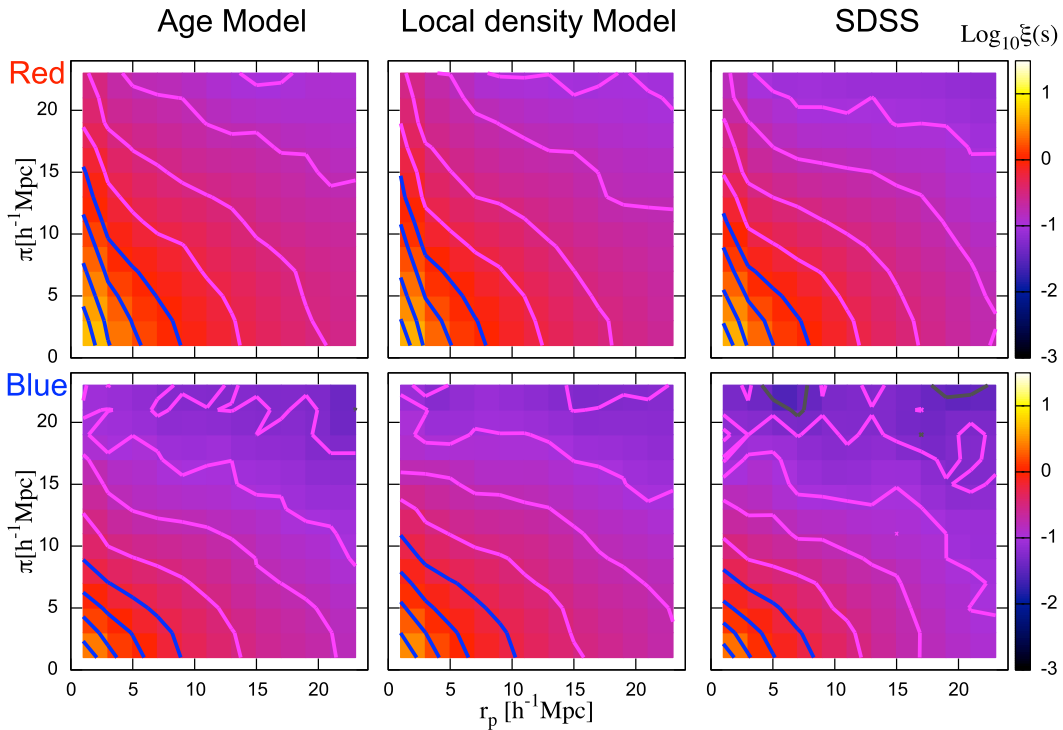


Figure 2. Color difference of the two dimensional correlation function $\xi(r_p, \pi)$ where r_p is the projected separation and π is the line-of-sight separation. Upper (Lower) panels show the results of red (blue) subhalos by separating color by the subhalo age (left) or the local DM density (center). Right panels show the observational results for comparison. All figures correspond to the sample with the intermediate magnitude range of $-21 < M_r < -20$.

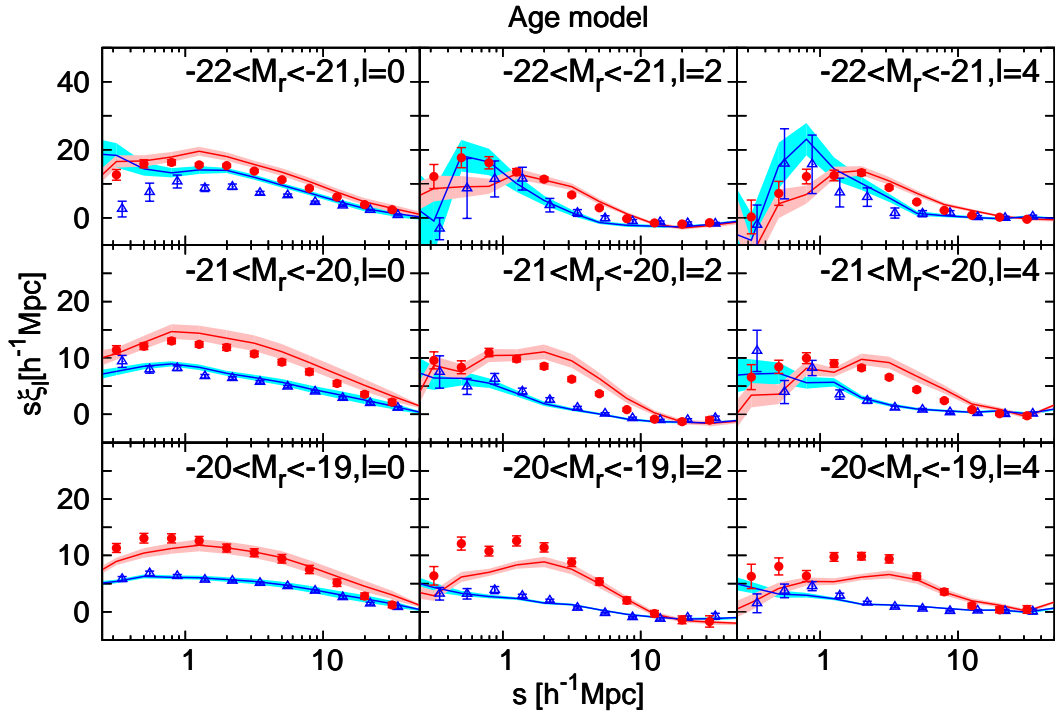


Figure 3. Comparison of the observed multipole correlation functions $\xi_l(s)$ ($l = 0, 2, 4$) for red and blue galaxies with those of simulated subhalo samples where the color is assigned by the subhalo age. Observational results for red and blue galaxies are plotted with filled circles and open triangles respectively. The simulation results are represented by the shade regions. Both errors of the observations and the simulations are estimated with the Jackknife resampling method.

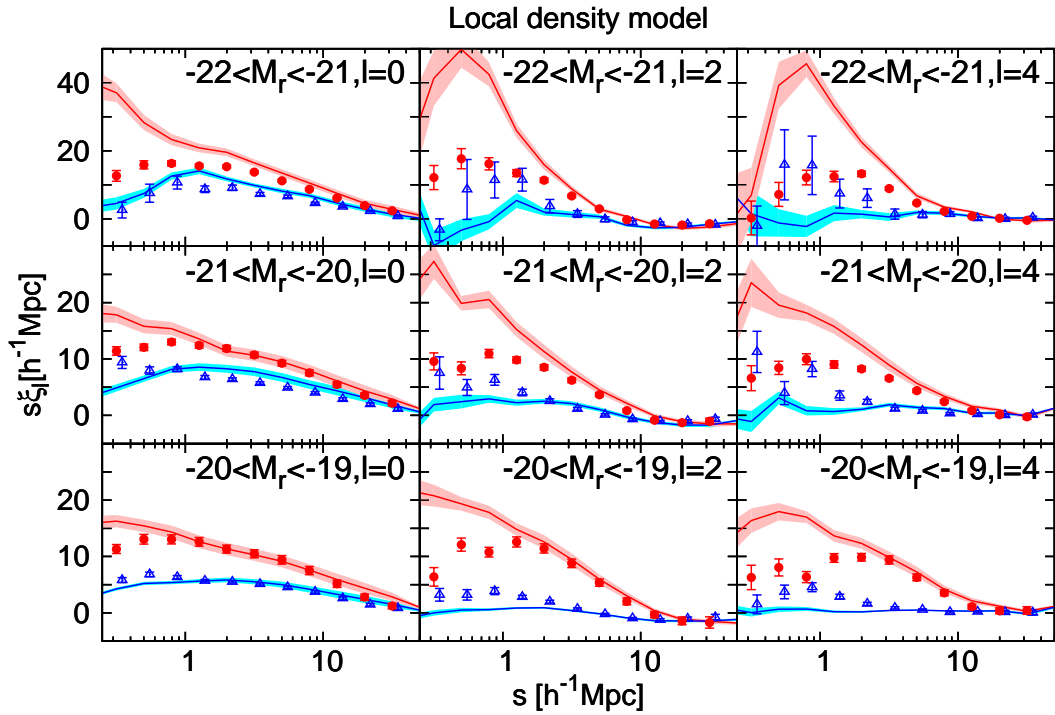


Figure 4. Same as Fig. 3 but for the color assignment based on the local DM density model.

is not included in N -body simulations. Hydrodynamical simulations show that baryonic components resist the tidal disruption of slowly-rotating subhalos and then decrease the averaged velocity of satellite subhalos (Faltenbacher et al. 2005; Wu et al. 2013). Our results may depend on the algorithms of finding subhalos. It would be interesting to apply other halo finders (e.g., Behroozi et al. 2013), however, these works are beyond the scope of our paper and we leave them to future works.

3.3 Color dependence: age model vs local DM density model

Next we see the color dependence of redshift-space clustering and test two color assignment models based on the subhalo age and the local DM density. Fig. 2 shows the two-dimensional correlation functions $\xi(r_p, \pi)$ where the distance of galaxy pairs are separated into the tangential separation r_p and the line-of-sight separation π . Upper (lower) panels show the results of red (blue) galaxies in the age model (left), the L.D. model (center), and observations (right) for the intermediate magnitude sample. Kaiser effect due to the coherent infalling motion squashes the galaxy distribution along the line-of-sight direction on large scale. On small scale around $1h^{-1}\text{Mpc}$, the FoG effect due to the internal motion of galaxies inside clusters elongates the distribution of galaxies along the line-of-sight direction. One can clearly see the color difference of the FoG effect in both color assigning models: red galaxies have a much stronger FoG effect than blue galaxies. This feature is consistent with the observational results for the SDSS galaxy samples in the right panels and also with the previous work done by Zehavi et al. (2011). One of the reasons is that red galaxy samples have a larger satellite fraction than blue ones as shown in Table 1. The internal velocity dispersion of red galaxies is also larger because red galaxies are hosted by massive halos. We make further discussion in the next subsection 3.4.

We make a more detailed comparison using a multipole expansion. Fig. 3 shows the measurements of monopole ($l = 0$), quadrupole ($l = 2$), and hexadecapole ($l = 4$) components for red and blue galaxies of the three magnitude samples. We find that the red galaxies have larger amplitudes than blue galaxies for all of the multipoles in our focused range of scales where the FoG effect is important. For comparison, we plot the results of subhalo samples with color assigned by the subhalo age. We find that the age model reproduces the color difference of redshift-space clustering down to subMpc scales very well. There are some systematic deviations: ξ_l for blue subhalos in the most luminous bin are stronger, but ξ_l for red subhalos in the faintest bin are weaker. The systematic trend is also seen before color separation (see Fig. 1 for comparison). This indicates that the discrepancy is mainly due to the incompleteness of SHAM not the color assignment scheme based on the subhalo age. We also compare the observations with the L.D. model in Fig. 4. In contrast to the age model, the L.D. model has significant deviations for all of the magnitude samples and multipoles at less than a few Mpc scale: red (blue) subhalos have too large (small) amplitude compared to the observations. This means that the color assignment by the local DM density is not enough to describe the redshift-space clustering and that the subhalo age is a much better proxy of galaxy color.

We evaluate the agreement of the multipole correlation functions between the observations and the subhalo samples in the chi-squared basis. The total χ^2 in each magnitude bin is computed by summing up the χ^2 for red and blue galaxies over different multipoles $l = 0, 2, \text{ and } 4$:

Table 2. Reduced chi-squared values of the multipole power spectra $\xi_l(l = 0, 2, 4)$ for three magnitude samples before color separation (“No color sep.”) and two color models (Age and L.D. model). Each chi-squared value is summed over three multipoles $l = 0, 2, \text{ and } 4$ and two colors after color separation. We adopt the range of scales is from $0.32 h^{-1}\text{Mpc}$ to $40 h^{-1}\text{Mpc}$ and the number of bins are 11 in the range. The total d.o.f. is 33 (or 66) before (or after) color separation.

M_r	$\chi^2/\text{d.o.f.}$		
	No color sep.	Age model	L.D. model
$[-22, -21]$	3.49	3.52	8.45
$[-21, -20]$	0.89	1.87	6.11
$[-20, -19]$	4.01	2.77	6.18

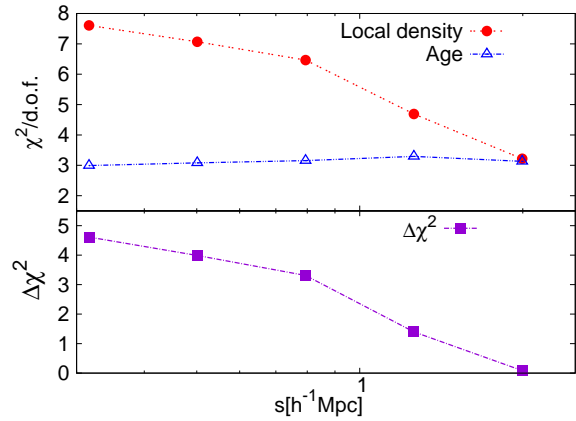


Figure 5. Comparison of the reduced chi-squared values between the age model and the L.D. model on different bins of scale s . Lower panel shows the difference of the chi-square $\Delta\chi^2$ between the two models.

$$\chi^2 = \sum_{\text{color}} \sum_{l=0,2,4} \sum_{s_{\min} < s_i < s_{\max}} \frac{[\xi_l^{\text{obs}}(s_i) - \xi_l^{\text{model}}(s_i)]^2}{\sigma_l^{\text{obs}, 2}(s_i) + \sigma_l^{\text{model}, 2}(s_i)}, \quad (5)$$

where $\sigma_l^{\text{obs}, 2}$, and $\sigma_l^{\text{model}, 2}$ are the variance of ξ_l for observations and subhalo samples estimated from the Jackknife method. The range of the fitting scale is from $s_{\min} = 0.32h^{-1}\text{Mpc}$ to $s_{\max} = 40h^{-1}\text{Mpc}$ with 11 bins. We neglect the covariance between different scales, multipoles and colors for simplicity.

Table 2 lists the reduced chi-squared values of three magnitude samples before and after color separation. The degrees-of-freedom (d.o.f.) of each magnitude bin is 33 (11 bins of scale \times 3 multipoles) before color separation and 66 after color separation. We find that the reduced χ^2 of the age model is 2-3. On the contrary, the L.D. model is significantly larger chi-squared values such as 6-8. Fig. 5 shows the comparison of the reduced χ^2 at each bin of scale on $\lesssim 1h^{-1}\text{Mpc}$ between the two color models. The fitting of the L.D. model is already worse around $1h^{-1}\text{Mpc}$ and then the deviation increases as the scale goes down.

3.4 Discussion

In the previous subsection, we find that the age model has a better agreement with the observed redshift-space clustering than the L.D. model. We here investigate why the two models have different features in the redshift-space clustering. The amplitude of ξ_l from subMpc to Mpc scale is mainly affected by the FoG effect, which

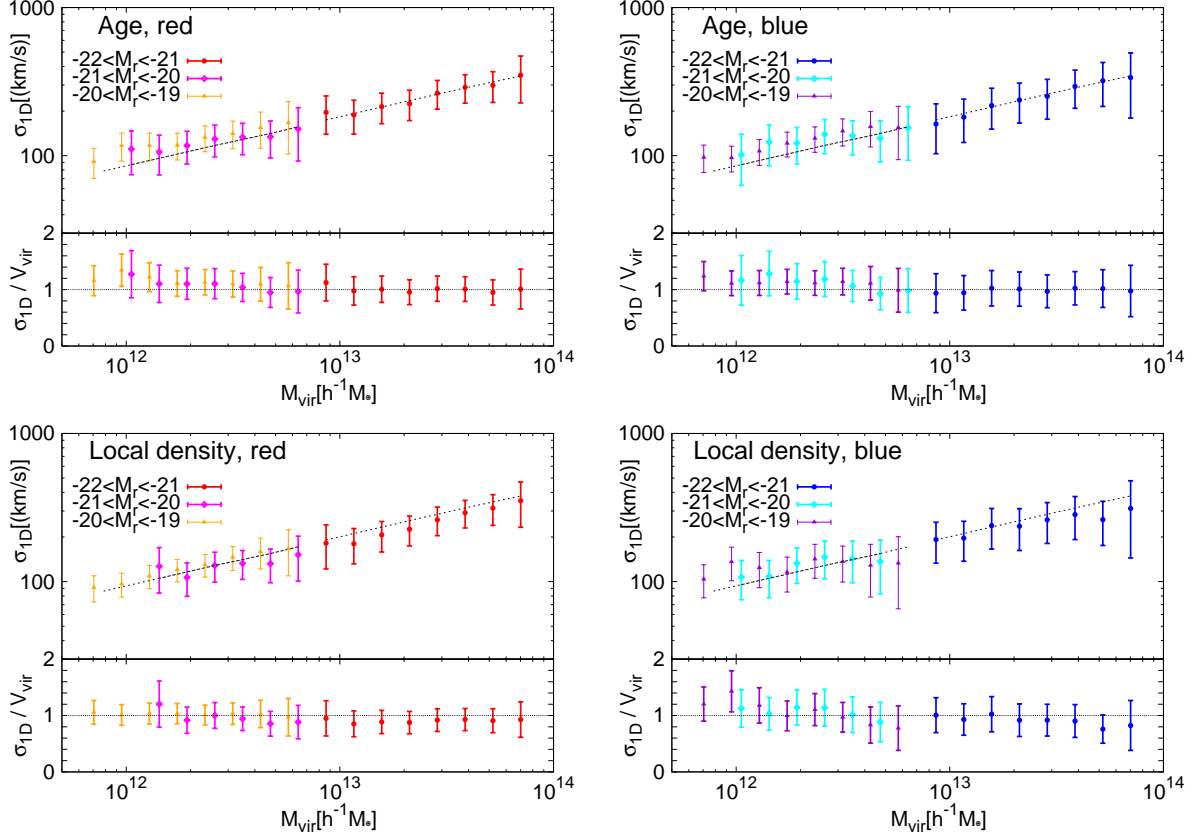


Figure 6. One-dimensional internal velocity dispersion σ_{1D} of red (left) and blue (right) satellite subhalos relative to the central subhalos as a function of the host halo mass for three magnitude samples. The color separation is based on the age (upper) and local DM density (lower) models respectively. For comparison, Virial velocity dispersion is plotted with lines. The error-bar represents 1σ dispersion in each bin of halo mass. The lower panels show the ratio σ_{1D}/σ_{vir} .

depends on the fraction of satellite galaxies, the internal velocity dispersion, and also the radial profile of satellites in their host halos. We here investigate where the differences between the models come from one by one.

As the satellite fraction increases, the contribution of central-satellite pairs and satellite-satellite pairs in the same halos increases, which generate the large amplitude of quadrupole and hexadecapole components on $\lesssim 1\text{Mpc}$. As shown in Table 1, however, the satellite fraction between the two color models is roughly same except for the faintest magnitude bin and thereby the number of satellites is not a main reason for the model difference of redshift-space clustering.

The FoG effect comes from the internal velocity dispersion, which is mainly dependent on the host halo mass. Table 3 lists the mean halo mass weighted with the number of satellite subhalos:

$$\langle M_{\text{halo}}^{\text{sat,wei}} \rangle = \frac{\sum_i M_{\text{halo},i} N_{\text{sat},i}}{\sum_i N_{\text{sat},i}}, \quad (6)$$

where $M_{\text{halo},i}$ and $N_{\text{sat},i}$ is the mass and the number of satellite subhalos in i -th halo. One can see that more luminous and redder satellites are hosted by more massive halos. We find that the difference of the host halo mass between colors is rather small in the L.D. model than the age model. It is thereby difficult to explain the large color difference of redshift-space clustering in the L.D. model.

We also see if the velocity dispersion of red and blue subhalos follow the expectations of Virial theorem. Fig. 6 shows the

Table 3. Comparison of the mean halo mass weighted with the number of satellite subhalos (eq.[6]) for the red and blue subhalo samples in the two color assignment models.

M_r	$\langle M_{\text{halo}}^{\text{sat,wei}} \rangle [10^{14} h^{-1} M_{\odot}]$			
	Age model		L.D. model	
	red	blue	red	blue
$[-22, -21]$	1.46	1.09	1.40	1.36
$[-21, -20]$	1.30	0.80	1.13	1.16
$[-20, -19]$	1.06	0.64	0.90	0.76

one-dimensional (1D) internal velocity dispersion of satellite subhalos as a function of the host halo mass in the age and L.D. model. Lines represent the Virial velocity dispersion estimated by $\sigma_{vir} = (GM_{vir}/2R_{vir})^{1/2}$ where M_{vir} and R_{vir} represent Virial mass and radius. The 1D velocity dispersion of satellite subhalos to the central subhalos are estimated as $|\mathbf{v}^{(\text{sat})} - \mathbf{v}^{(\text{cen})}|^2/3$. The error-bars represent the $1-\sigma$ dispersion in each bin of halo mass. In both models, we find that the satellite velocity dispersions agree with the expectations from Virial theorem within the error bars irrespective of color, though dispersion slightly decreases as the host halo is more massive. The velocity dispersion is unlikely to explain the difference of redshift-space clustering between the two models.

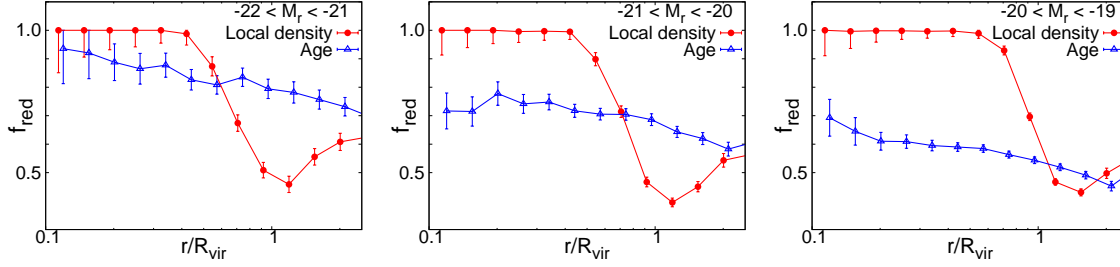


Figure 7. The fraction of red galaxies as a function of the distance from the host halo center normalized by the Virial radius R_{vir} for three magnitude samples. Red and blue lines represent the results for the L.D. model and the age model respectively. The error-bar represents the Poisson error in each bin of scale.

Finally we see the radial profile of satellites which affect the small-scale clustering. Fig. 7 shows that the fraction of red galaxies $f_{\text{red}} \equiv N_{\text{red}}/(N_{\text{red}} + N_{\text{blue}})$ as a function of the distance R from the halo center normalized by the Virial radius R_{vir} in the three magnitude samples. For all of the samples, there is a clear difference between the two color models. The red fraction in the age model slightly decreases at larger R , whereas the red fraction in the L.D. model is almost unity inside the host halo and drastically declines around the Virial radius. This can explain the big difference between colors in the redshift-space clustering: a large number of red galaxy pairs inside halos causes too strong FoG effect, however, the lack of blue galaxies have too weak FoG. The observed red fraction actually shows a similar trend to the age model (Hansen et al. 2009). This means that the color assignment in the L.D. model is too simple to describe the color difference of galaxy clustering inside halos.

We investigate how the result changes by including scatter in the color assignment. Instead of assuming the monotonic relation between the color and ρ_{DM} , we assign red color to the subhalo with the local DM density of ρ_{DM} in the following probability:

$$P_{\text{red}}(\rho_{\text{DM}}) = \frac{1}{2} \left[1 + \text{erf} \left(\frac{\log_{10}(\rho_{\text{DM}}/\rho_{\text{DM}}^{\text{thre}})}{\sigma_{\log \rho}} \right) \right], \quad (7)$$

where erf is the error function, $\rho_{\text{DM}}^{\text{thre}}$ is a threshold density dividing red and blue colors without scatter to match the observed red fraction, and $\sigma_{\log \rho}$ denotes the scatter in logarithmic scale of ρ_{DM} . Fig. 8 shows the comparison of observed quadrupole components of the intermediate sample with the corresponding measurements in the L.D. model by varying $\sigma_{\log \rho}$ as 0.2, 0.3, and 0.4. We change the parameter of R_{DM} to be 600 kpc to agree with the observed projected correlation functions (Masaki et al. 2013b). Introducing an appropriate scatter improves the agreement with the observations. We find that the scatter value of $\sigma_{\log \rho}$ around 0.3 has a best agreement in blue samples, while $\sigma_{\log \rho}$ between 0.3 and 0.4 is best for red samples. The chi-squared value for the $\sigma_{\log \rho} = 0.3(0.4)$ significantly decreases to be 3.62(4.55) compared to the no-scatter case of 6.11(6.18) in Table 2. The agreement in the age model is still better than the L.D. model even when the scatter is included. This is because the introduction of scatter in the form of eq. [7] cannot reproduce the clustering of red and blue galaxy samples simultaneously. This implies that the age model is much better color assignment than the L.D. model and then the subhalo age is a key ingredient to determine the color of galaxies.

4 SUMMARY AND CONCLUSIONS

We extend the SHAM approach to redshift space and test if the SHAM explain the luminosity and color dependence of the redshift-space clustering. We find that the simple subhalo abundance matching using monotonic relation between the galaxy luminosity to the maximum circular velocity qualitatively well reproduces the luminosity dependence of SDSS galaxy clustering from $0.3 h^{-1}\text{Mpc}$ to $40 h^{-1}\text{Mpc}$. This indicates that the satellite motion inside clusters is mainly determined with that of the host subhalos. Our results indicate that the SHAM method can be applied for RSD studies and provides a promising way to construct mock samples of redshift-space galaxy distribution. There is however a systematic difference on subMpc scale and then the effect of baryonic physics may be necessary to be included to achieve more precise theoretical modeling for future galaxy surveys.

In addition to the luminosity dependence, we also apply two methods of color abundance matching where the color is assigned by the age of subhalos and the local DM density. We find that the color assignment by the subhalo age much better agrees with the observations than by the local DM density. The main reason why the local density model fails to reproduce the observed clustering is that the fraction of red subhalos in the model is too large inside the host halos. The agreement improves by introducing a scatter in the relation between color and local DM density, but still the color assignment based on the subhalo age has better chi-squared values. This suggests that the subhalo age is a main driver of determining the color of galaxies and a key ingredient to make an accurate mock galaxy samples with different colors.

Our analysis using redshift-space clustering prefers the age model to the local density model. This is apparently inconsistent with the galaxy-galaxy lensing analysis by Masaki et al. (2013b), which support the local DM density model. This is because the redshift-space clustering and lensing are sensitive to different aspects of the galaxy clustering: the redshift-space clustering, in particular the FoG effect, is sensitive to the satellite properties such as the satellite profile and dynamics. On the other hand, galaxy-galaxy lensing probes the averaged halo mass hosting all of the galaxies in a given sample. This means that both of the color assignment models still need to be improved.

In this analysis, we assume that the central galaxy sit on the halo center and neglect the internal velocity relative to the host halo bulk velocity. Recent analysis using the Baryonic Oscillation Spectroscopic Survey (BOSS) CMASS data shows that the central galaxies may have $\sim 30\%$ of the Virial velocity (Guo et al. 2015). This increases the velocity dispersion between central galaxies and satellite galaxies at $\sim 9\%$ ($\sim 0.3^2$). Baryon components also affect the dynamics of satellite galaxies. The mean velocity of satellites decrease by including baryonic components which pre-

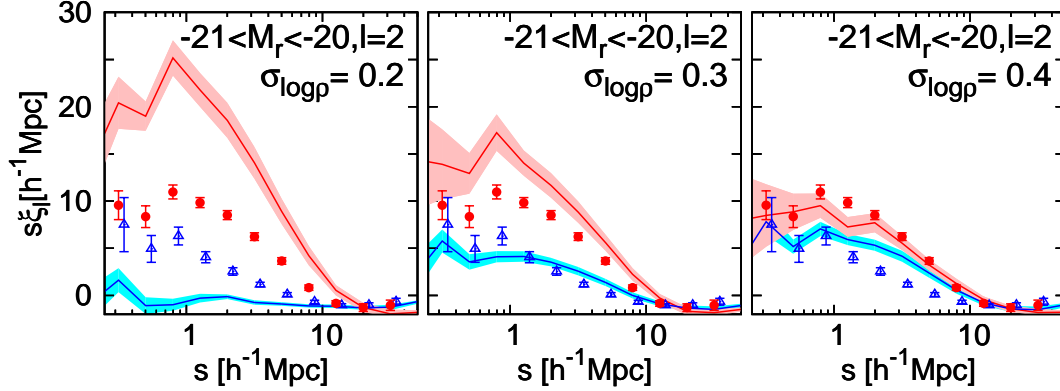


Figure 8. Comparison of observed quadrupole component ξ_2 for red and blue galaxies based on the L.D. model. The scatter in the color assignment is included as the equation 7 and the logarithmic scatter value $\sigma_{\log \rho}$ is 0.2, 0.3, and 0.4 from left to right panels.

vents the tidal disruption of slow subhalos by 10 percent level (Faltenbacher et al. 2005; Wu et al. 2013). It may be also interesting to see how our result changes using different algorithms of identifying subhalos. We leave further detailed analysis as a future work.

ACKNOWLEDGMENTS

CH acknowledges support from a Grant-in-Aid for Scientific Research from the Ministry of Education, Science, Sports, and Culture, Japan, No. 24740160.

REFERENCES

- Abazajian K. N., Adelman-McCarthy J. K., Agüeros M. A., Allam S. S., Allende Prieto C., An D., Anderson K. S. J., Anderson S. F., Annis J., Bahcall N. A., et al., 2009, *ApJS*, 182, 543
- Balogh M. L., Baldry I. K., Nichol R., Miller C., Bower R., Glazebrook K., 2004, *ApJ*, 615, L101
- Bamford S. P., Nichol R. C., Baldry I. K., Land K., Lintott C. J., Schawinski K., Slosar A., Szalay A. S., Thomas D., Torri M., Andreescu D., Edmondson E. M., Miller C. J., Murray P., Radcliff M. J., Vandenberg J., 2009, *MNRAS*, 393, 1324
- Behroozi P. S., Wechsler R. H., Conroy C., 2013, *ApJ*, 770, 57
- Beutler F., Saito S., Seo H.-J., Brinkmann J., Dawson K. S., Eisenstein D. J., Font-Ribera A., Ho S., McBride C. K., Montesano F., Percival W. J., Ross A. J., Ross N. P., Samushia L., Schlegel D. J., Sánchez A. G., Tinker J. L., Weaver B. A., 2014, *MNRAS*, 443, 1065
- Blanton M. R., Berlind A. A., 2007, *ApJ*, 664, 791
- Coil A. L., Newman J. A., Croton D., Cooper M. C., Davis M., Faber S. M., Gerke B. F., Koo D. C., Padmanabhan N., Wechsler R. H., Weiner B. J., 2008, *ApJ*, 672, 153
- Conroy C., Wechsler R. H., 2009, *ApJ*, 696, 620
- Conroy C., Wechsler R. H., Kravtsov A. V., 2006, *ApJ*, 647, 201
- Cooper M. C., Newman J. A., Croton D. J., Weiner B. J., Willmer C. N. A., Gerke B. F., Madgwick D. S., Faber S. M., Davis M., Coil A. L., Finkbeiner D. P., Guhathakurta P., Koo D. C., 2006, *MNRAS*, 370, 198
- Faltenbacher A., Kravtsov A. V., Nagai D., Gottlöber S., 2005, *MNRAS*, 358, 139
- Guo H., Zheng Z., Zehavi I., Dawson K., Skibba R. A., Tinker J. L., Weinberg D. H., White M., Schneider D. P., 2015, *MNRAS*, 446, 578
- Guo H., Zheng Z., Zehavi I., Xu H., Eisenstein D. J., Weinberg D. H., Bahcall N. A., Berlind A. A., Comparat J., McBride C. K., Ross A. J., Schneider D. P., Skibba R. A., Swanson M. E. C., Tinker J. L., Tojeiro R., Wake D. A., 2014, *MNRAS*, 441, 2398
- Guzzo L., et al., 2008, *Nature*, 451, 541
- Hamilton A. J. S., 1992, *ApJ*, 385, L5
- Hansen S. M., Sheldon E. S., Wechsler R. H., Koester B. P., 2009, *ApJ*, 699, 1333
- Hearin A. P., 2015, *ArXiv e-prints*
- Hearin A. P., Watson D. F., 2013, *MNRAS*, 435, 1313
- Hikage C., 2014, *MNRAS*, 441, L21
- Hikage C., Yamamoto K., 2013, *JCAP*, 8, 19
- Jackson J. C., 1972, *MNRAS*, 156, 1P
- Kaiser N., 1987, *MNRAS*, 227, 1
- Komatsu E., Smith K. M., Dunkley J., Bennett C. L., Gold B., Hinshaw G., Jarosik N., Larson D., Nolte M. R., Page L., Spergel D. N., Halpern M., Hill R. S., Kogut A., Limon M., Meyer S. S., Odegard N., Tucker G. S., Weiland J. L., Wollack E., Wright E. L., 2011, *ApJS*, 192, 18
- Kravtsov A. V., Berlind A. A., Wechsler R. H., Klypin A. A., Gottlöber S., Allgood B., Primack J. R., 2004, *ApJ*, 609, 35
- Landy S. D., Szalay A. S., 1993, *ApJ*, 412, 64
- Laureijs R., Amiaux J., Arduini S., Auguères J., Brinchmann J., Cole R., Cropper M., Dabin C., Duvet L., Ealet A., et al., 2011, *ArXiv e-prints*
- Leauthaud A., Finoguenov A., Kneib J.-P., Taylor J. E., Massey R., Rhodes J., Ilbert O., Bundy K., Tinker J., George M. R., Capak P., Koekemoer A. M., Johnston D. E., Zhang Y.-Y., Cappelluti N., Ellis R. S., Elvis M., Giodini S., Heymans C., Le Fèvre O., Lilly S., McCracken H. J., Mellier Y., Réfrégier A., Salvato M., Scoville N., Smoot G., Tanaka M., Van Waerbeke L., Wolk M., 2010, *ApJ*, 709, 97
- Levi M., Bebek C., Beers T., Blum R., Cahn R., Eisenstein D., Flaugher B., Honscheid K., Kron R., Lahav O., McDonald P., Roe N., Schlegel D., representing the DESI collaboration, 2013, *ArXiv e-prints*
- Mandelbaum R., Seljak U., Cool R. J., Blanton M., Hirata C. M., Brinkmann J., 2006, *MNRAS*, 372, 758
- Masaki S., Hikage C., Takada M., Spergel D. N., Sugiyama N., 2013a, *MNRAS*, 433, 3506
- Masaki S., Lin Y.-T., Yoshida N., 2013b, *MNRAS*, 436, 2286

- Nagai D., Kravtsov A. V., 2005, *ApJ*, 618, 557
- Norberg P., Baugh C. M., Hawkins E., Maddox S., Madgwick D., Lahav O., Cole S., Frenk C. S., Baldry I., Bland-Hawthorn J., Bridges T., Cannon R., Colless M., Collins C., Couch W., Dalton G., De Propris R., Driver S. P., Efstathiou G., Ellis R. S., Glazebrook K., Jackson C., Lewis I., Lumsden S., Peacock J. A., Peterson B. A., Sutherland W., Taylor K., 2002, *MNRAS*, 332, 827
- Peacock J. A., et al., 2001, *Nature*, 410, 169
- Skibba R. A., Smith M. S. M., Coil A. L., Moustakas J., Aird J., Blanton M. R., Bray A. D., Cool R. J., Eisenstein D. J., Mendez A. J., Wong K. C., Zhu G., 2014, *ApJ*, 784, 128
- Spergel D., Gehrels N., Breckinridge J., Donahue M., Dressler A., Gaudi B. S., Greene T., Guyon O., Hirata C., Kalirai J., Kasdin N. J., Moos W., Perlmutter S., Postman M., Rauscher B., Rhodes J., Wang Y., Weinberg D., Centrella J., Traub W., Baltay C., Colbert J., Bennett D., Kiessling A., Macintosh B., Merten J., Mortonson M., Penny M., Rozo E., Savransky D., Stapelfeldt K., Zu Y., Baker C., Cheng E., Content D., Dooley J., Foote M., Goullioud R., Grady K., Jackson C., Kruk J., Levine M., Melton M., Peddie C., Ruffa J., Shaklan S., 2013, *ArXiv e-prints*
- Springel V., 2005, *MNRAS*, 364, 1105
- Springel V., White S. D. M., Tormen G., Kauffmann G., 2001a, *MNRAS*, 328, 726
- Springel V., Yoshida N., White S. D. M., 2001b, *NewA*, 6, 79
- Takada M., Ellis R., Chiba M., Greene J. E., Aihara H., Arimoto N., Bundy K., Cohen J., Doré O., Graves G., Gunn J. E., Heckman T., Hirata C., Ho P., Kneib J.-P., Le Fèvre O., Lin L., More S., Murayama H., Nagao T., Ouchi M., Seiffert M., Silverman J., Sodré Jr L., Spergel D. N., Strauss M. A., Sugai H., Suto Y., Takami H., Wyse R., 2012, *ArXiv e-prints*
- Wu H.-Y., Hahn O., Evrard A. E., Wechsler R. H., Dolag K., 2013, *MNRAS*, 436, 460
- Yamamoto K., Nakamura G., Hütsi G., Narikawa T., Sato T., 2010, *Phys. Rev. D*, 81, 103517
- Yamamoto K., Sato T., Hütsi G., 2008, *Progress of Theoretical Physics*, 120, 609
- Zehavi I., Eisenstein D. J., Nichol R. C., Blanton M. R., Hogg D. W., Brinkmann J., Loveday J., Meiksin A., Schneider D. P., Tegmark M., 2005, *ApJ*, 621, 22
- Zehavi I., Zheng Z., Weinberg D. H., Blanton M. R., Bahcall N. A., Berlind A. A., Brinkmann J., Frieman J. A., Gunn J. E., Lupton R. H., Nichol R. C., Percival W. J., Schneider D. P., Skibba R. A., Strauss M. A., Tegmark M., York D. G., 2011, *ApJ*, 736, 59